How to cite: *Angew. Chem. Int. Ed.* **2023**, *62*, e202305212
doi.org/10.1002/anie.202305212

Covalent Organic Frameworks | Hot Paper

Dual Microenvironment Modulation of Pd Nanoparticles in Covalent Organic Frameworks for Semihydrogenation of Alkynes

*Mingchun Guo, Qiangqiang Meng, Wenyao Chen, Zheng Meng, Ming-Liang Gao, Qunxiang Li, Xuezhi Duan, and Hai-Long Jiang**

Abstract: The chemical microenvironment modulation of metal nanoparticles (NPs) holds promise for tackling the long-lasting challenge of the trade-off effect between activity and selectivity in catalysis. Herein, ultrafine $PdCu_2$ NPs incorporated into covalent organic frameworks (COFs) with diverse groups on their pore walls have been fabricated for the semihydrogenation of alkynes. The Cu species, as the primary microenvironment of Pd active sites, greatly improves the selectivity. The functional groups as the secondary microenvironment around $PdCu_2$ NPs effectively regulate the activity, in which $PdCu_2$ NPs encapsulated in the COF bearing $-CH_3$ groups exhibit the highest activity with >99% conversion and 97% selectivity. Both experimental and calculation results suggest that the functional group affects the electron-donating ability of the COFs, which successively impacts the charge transfer between COFs and Pd sites, giving rise to a modulated Pd electronic state and excellent catalytic performance.

Introduction

Styrene is one of the most important monomers in producing polystyrene. In the polystyrene production industry, the presence of phenylacetylene reduces the quality of styrene products; therefore, the selective hydrogenation of phenylacetylene to styrene is a critical solution in this process.[1] At present, Pd nanoparticles (NPs) are the most commonly used in hydrogenation reactions due to their excellent H_2 activation ability.[1f,g] However, overhydrogenation of the C=C bond often occurs over Pd-based catalysts. Due to styrene on Pd NPs is difficult to desorb in time, thus causing excessive hydrogenation. Therefore, alloying Cu with Pd might effectively increase the selectivity to styrene by regulating the electronic structure of Pd via charge transfer to change the *d*-band center location of Pd.[2] On the other hand, small Pd NPs exhibit great potential in catalytic performance; however, owing to their high surface energy, they are prone to aggregation in the catalytic process, which significantly diminishes their activity and reusability in practical applications.[3] To overcome this limitation, two common approaches have been adopted. The first approach relies on the introduction of ligands or surfactants as protectors for Pd NPs.[4] Unfortunately, the introduced protectors may also mask the Pd sites to a certain degree, leading to reduced activity. The second approach is the incorporation of Pd NPs into suitable porous scaffolds, i.e., metal–organic frameworks (MOFs), zeolites, porous carbons, etc.[5] Despite being promising in Pd confinement using porous materials, the trade-off between good selectivity and high activity/stability is usually observed due to the lack of electronic state control of Pd NPs after their incorporation into the scaffolds. Actually, a suitable Pd electronic state would facilitate alkyne activation while inhibiting the overhydrogenation of the C=C bond,[6] which is highly demanded to target an optimal balance of high activity and selectivity. To this end, it is expected to adopt stable, well-defined, and readily tailorable hosts with engineered pore walls that serve as microenvironment to precisely tailor the Pd electronic state for enhanced activity and selectivity.

In this context, covalent organic frameworks (COFs), a class of crystalline porous polymers featuring high surface area, tunable pore size, and high compositional and structural tailorability, are very promising candidates.[7] Their customizable pore structures are able to serve as ideal hosts for the confinement and stabilization of small metal NPs meanwhile providing adequate access to the substrates.[8] More importantly, the great tailorability of COFs makes it feasible to modulate the microenvironment around Pd sites via pore wall engineering. The modular and well-defined nature of COFs allows the implementation of pore wall engineering in a rational and systematic manner, which is beneficial to the understanding of the structure–property relationship. Moreover, by dangling diverse groups onto the pore walls of the COF skeleton is expected to regulate Pd electronic properties based on the differentiated chemical

[*] M. Guo, Prof. Dr. Z. Meng, Dr. M.-L. Gao, Prof. Dr. H.-L. Jiang
Hefei National Research Center for Physical Sciences at the Microscale, Department of Chemistry, Collaborative Innovation Center of Chemistry for Energy Materials (iChEM), University of Science and Technology of China
Hefei, Anhui 230026 (P. R. China)
E-mail: jianglab@ustc.edu.cn
Homepage: http://mof.ustc.edu.cn/
Dr. Q. Meng, Prof. Dr. Q. Li
Department of Chemical Physics, University of Science and Technology of China
Hefei, Anhui 230026 (P. R. China)
Dr. W. Chen, Prof. Dr. X. Duan
State Key Laboratory of Chemical Engineering, East China University of Science and Technology
130 Meilong Road, Shanghai 200237 (P. R. China)

nature of various groups. Therefore, the structural features of COFs provide an ideal platform for protecting Pd NPs and modulating their electronic properties precisely, which would overcome the limitations in conventional incorporation of Pd NPs and lead to the expected activity and selectivity in the hydrogenation of alkynes.

Based on the above considerations, in this work, a series of COFs with different functional groups dangling on the pore wall, named MF–X (X = –CH_3, –H, –CF_3, and –CN),[9] have been fabricated. The $PdCu_2$ alloy NPs are incorporated into MF–X to afford $PdCu_2$@MF–X for the semihydrogenation of phenylacetylene to styrene (Scheme 1). The Pd sites are responsible for the conversion, yet the alloyed Cu species in the first coordination sphere of Pd, serving as the primary (proximate) microenvironment, greatly improve the selectivity. Meanwhile, the interaction between Pd NPs and the functional groups on the COF pore wall serving as a secondary (remote) microenvironment significantly modulates the Pd electronic state, leading to discriminated activity. The optimized $PdCu_2$@MF–CH_3 achieves excellent compatibility between activity and selectivity with >99% conversion and selectivity up to 97% in the semihydrogenation of phenylacetylene to styrene, and it can be extended to diverse terminal alkynes. Both experimental results and theoretical simulations suggest that the interaction of Pd with the electron-donating group –CH_3 increases the Pd electron density, thereby improving the hydrogenation activity. Our strategy provides a guideline for the rational design of COF-based catalysts with high activity, selectivity, and stability toward the semihydrogenation of a wide range of alkynes under mild conditions.

Results and Discussion

The Povarov cycloaddition between the presynthesized TAPB-DMTA-COF and *para*-substituted aryl alkynes under similar conditions (see Supporting Information for details) leads to the formation of MF–X (X = –CH_3, –H, –CF_3 and –CN) with diverse functional groups decorated on the COF pore walls.[9] Powder X-ray diffraction (XRD) profiles of TAPB-DMTA-COF and MF–X display similar patterns, demonstrating that the COFs present high crystallinity and the skeleton is maintained after the Povarov reaction (Figure S1). In the infrared (IR) spectra of MF–X, strong peaks at 1541 and 1580 cm^{-1} appear accompanied by the attenuation of the C=N peak intensity at 1614 cm^{-1}, which supports the successful conversion of C=N to quinolyl species (Figure S2). Meanwhile, the characteristic peaks ascribed to the –CH_3 stretch (~2900 cm^{-1}), –CN vibration (~2231 cm^{-1}), and –CF_3 stretch (~1325 cm^{-1}) can be clearly identified for MF–CH_3, MF–CN, and MF–CF_3, respectively (Figure S2). In addition, the fraction of N 1s shifts to a lower binding energy of 398.5 eV after the Povarov reaction, which can further support the formation of quinolyl species. Meanwhile, the new peak appearing at 399.5 eV is associated with quinoline (Figure S3).[10] Based on the peak area of imine and quinoline in the N 1s XPS spectra of MF–CH_3, MF–H, MF–CF_3 and MF–CN, the conversion degree can be evaluated to be 43%, 41%, 38% and 45%, respectively. These results demonstrate the successful attachment of -X groups with similar loadings in the COF skeleton.

The Pd and $PdCu_2$ NPs were then incorporated into the MF–X with incipient wetness impregnation followed by H_2 reduction (see Supporting Information for details). Powder XRD results suggest that all $PdCu_2$@MF–X and Pd@MF–CH_3 samples inherit the phase purity and crystallinity of MF–X well (Figure 1a). Nitrogen sorption experi-

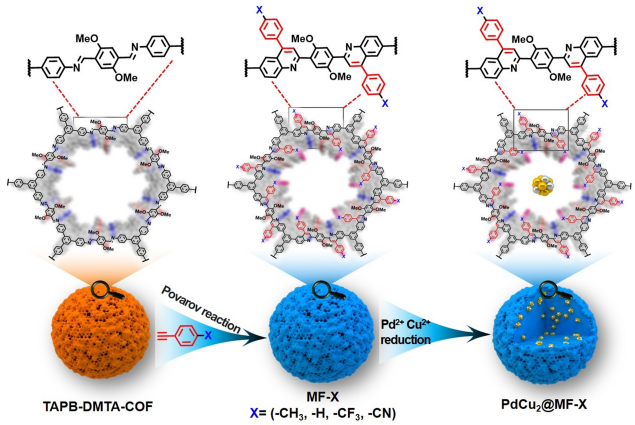

Scheme 1. Schematic illustration showing the stepwise synthesis of $PdCu_2$@MF–X (X = –CH_3, –H, –CF_3, –CN) catalysts.

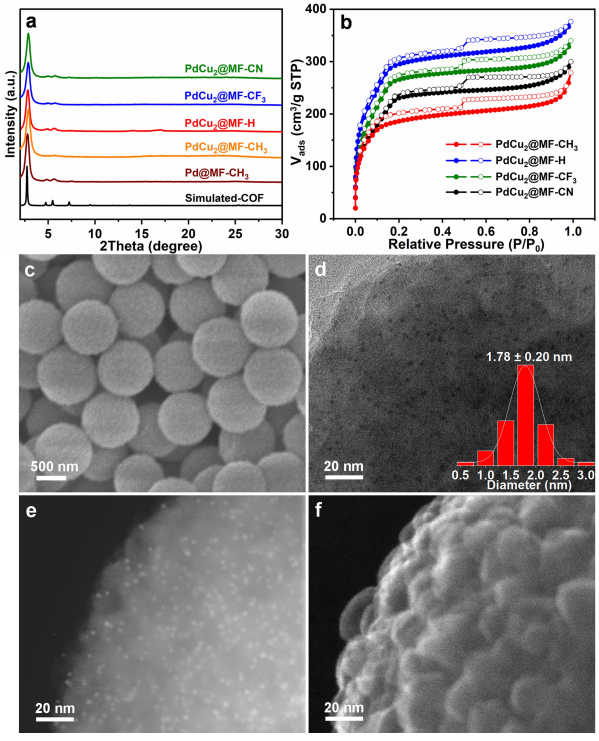

Figure 1. a) Powder XRD patterns of Pd@MF–CH_3 and $PdCu_2$@MF–X samples. b) N_2 sorption isotherms for $PdCu_2$@MF–X at 77 K. c) SEM and d) TEM images of $PdCu_2$@MF–CH_3 (inset: size distribution of $PdCu_2$ NPs). e) HAADF-STEM and f) SE-STEM images of $PdCu_2$@MF–CH_3.

ments reveal Brunauer–Emmett–Teller (BET) surface areas in the range of 590–959 $m^2 g^{-1}$ for $PdCu_2$@MF–X, where the slight decrease compared to their corresponding parent MF–X is likely ascribed to the mass and pore occupation by the $PdCu_2$ NPs (Figures 1b, S4).[11] Meanwhile, the specific BET surface areas, pore volumes and pore size distributions of MF–X before and after the incorporation of $PdCu_2$ NPs are summarized (Figure S5, Table S1). As evaluated by inductively coupled plasma atomic emission spectrometry (ICP–AES), the Pd and Cu contents in $PdCu_2$@MF–X remain consistent, where the Pd contents are in the range of 0.97–1.09 wt %, close to that in Pd@MF–CH_3, and the Cu contents are in the range of 1.13–1.24 wt % (Table S2), indicating that the molar ratio of Pd and Cu is close to 1:2 in $PdCu_2$@MF–X, in line with the energy-dispersive X-ray (EDX) analysis results (Figure S6). Scanning electron microscopy (SEM) observation shows that Pd@MF–CH_3 and $PdCu_2$@MF–X all possess uniform spherical morphology with an average diameter of ~1.0 μm (Figures 1c, S7). Transmission electron microscopy (TEM) observation for $PdCu_2$@MF–CH_3 suggests that ultrafine $PdCu_2$ NPs with a mean size of ~1.78 nm are highly dispersed throughout the COF particle (Figure 1d), which are in similar sizes of Pd NPs in Pd@MF–CH_3, $PdCu_2$@MF–H, $PdCu_2$@MF–CF_3 and $PdCu_2$@MF–CN (Figure S8). To gain solid evidence on the location of $PdCu_2$ NPs relative to the COF particle, direct comparison of HAADF-STEM and secondary electron scanning transmission electron microscopy (SE-STEM) images for the same particles has been conducted. The observation shows that $PdCu_2$ NPs in the HAADF-STEM image (Figure 1e) at the same position are barely observable in SE-STEM image (Figure 1f) for $PdCu_2$@MF–CH_3, unambiguously demonstrate that $PdCu_2$ NPs are basically located inside the COF pores, which is in good agreement with the decreased N_2 sorption of $PdCu_2$@MF–X. The thermogravimetric analysis (TGA) trace indicates that $PdCu_2$@MF–X remains intake up to a temperature of over 400 °C, suggesting its good thermal stability (Figure S9).

Encouraged by the above characterizations, phenylacetylene is firstly chosen as the model substance to investigate the semihydrogenation performance over $PdCu_2$@MF–X at 30 °C and 1 bar of H_2 atmosphere. As expected, Pd@MF–CH_3 efficiently achieves the hydrogenation of phenylacetylene, yet its overhydrogenation quickly takes place, generating an unexpected phenylethane product (Figure S10). The selectivity can be improved to 95 % at the beginning stage of the reaction by adding a small amount of pyridine based on previous reports,[12] but it gradually decreases to 90 % when prolonging the reaction time (Figure S11a). The performance of Pd@MF–X in the semihydrogenation of phenylacetylene has also been examined by adding a similar amount of pyridine. Similarly, none of their selectivity can be maintained when prolonging the reaction time (Figure S11b–d). To our surprise, when introducing Cu to tailor the coordination microenvironment of Pd sites, the system gets improved and gives almost retained selectivity in the presence of pyridine. Screening experiments on different Cu amounts demonstrate that $PdCu_2$@MF–CH_3 with a Pd/Cu molar ratio of 1:2 in the presence of pyridine exhibits satisfactory conversion (> 99 %) and selectivity (97 %) to targeted styrene, even with a prolonged reaction time of 8 h (Figure 2a). These results reveal the possible synergistic effect between Cu and pyridine for high selectivity. It is worth noting that overhydrogenation over $PdCu_2$@MF–CH_3 can be observed at high conversion in the prolonged reaction time in the absence of pyridine (Figure S12), supporting the importance of pyridine in the system.

Given the satisfactory selectivity achieved by $PdCu_2$ NPs, we then set out to investigate the catalysis over $PdCu_2$@MF–X in the semihydrogenation of phenylacetylene. In comparison to the primary microenvironment of Cu species for Pd sites, the X functional groups on the COF pore walls create a secondary microenvironment for $PdCu_2$ NPs, which is supposed to further affect the performance in the catalytic reaction. As expected, although all $PdCu_2$@MF–X exhibit similarly high selectivity to styrene (97 %), their activities are distinctly different, which follow the order of $PdCu_2$@MF–CN < $PdCu_2$@MF–CF_3 < $PdCu_2$@MF–H < $PdCu_2$@MF–CH_3 (Figure 2b). The secondary microenvironment created by different functional groups around $PdCu_2$ sites should be responsible for the observed activity difference of $PdCu_2$@MF–X. In sharp contrast to the 18 % conversion for $PdCu_2$@MF–CN, a > 99 % conversion is achieved by $PdCu_2$@MF–CH_3 under the same conditions (Figure 2b). To our delight, among different reported catalysts toward the semihydrogenation

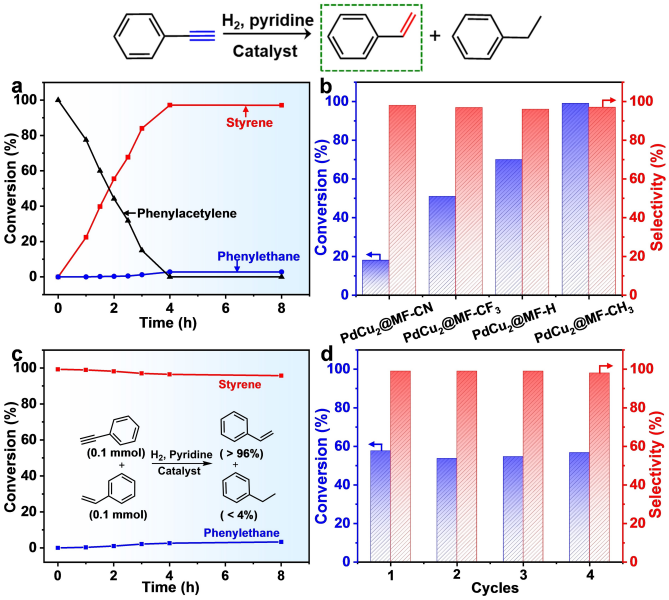

Figure 2. a) Time-dependent conversion in the hydrogenation of phenylacetylene over $PdCu_2$@MF–CH_3. b) Catalytic activity and selectivity of $PdCu_2$@MF–X for phenylacetylene semihydrogenation. c) Conversion and selectivity to styrene in phenylacetylene hydrogenation with a mixture (molar ratio of 1:1) of phenylacetylene and styrene over $PdCu_2$@MF–CH_3. d) Recycling performance of $PdCu_2$@MF–CH_3 in the semihydrogenation of phenylacetylene (reaction conditions: 30 °C for 2 h under 1 bar H_2 in the presence of pyridine).

of phenylacetylene (Table S3), $PdCu_2$@MF–CH_3 presents superior activity and selectivity.

To illustrate the high selectivity of $PdCu_2$@MF–CH_3 in the semihydrogenation of phenylacetylene, hydrogenation using a 1:1 mixture of phenylacetylene and styrene as substrates has been carried out (Figure 2c). Significantly, the presence of styrene does not influence the semihydrogenation of phenylacetylene into styrene. Recycling experiments for $PdCu_2$@MF–CH_3 show that its activity and selectivity can be well maintained at different conversions in four consecutive cycles, indicating good stability and reusability of the catalyst (Figure 2d, S13). Consistently, powder XRD profiles demonstrate that MF–X maintains high crystallinity and structural integrity after the catalytic reaction (Figure S14a). Meanwhile, the good dispersion of $PdCu_2$ NPs throughout the COF particles after the reaction has also been supported by TEM observations (Figure S14b). In addition, the hot filtration experiments for $PdCu_2$@MF–CH_3 indicate that no further conversion of phenylacetylene occurs upon the removal of the catalyst, reflecting the truly heterogeneous feature of the catalytic process; no Pd and Cu leaching can be found based on the ICP–AES results after reaction (Figure S15, Table S2, entry 6).

Encouraged by the excellent catalytic performance of $PdCu_2$@MF–CH_3 in the semihydrogenation of phenylacetylene, its applicability to the hydrogenation of diverse terminal alkynes, including aromatic alkynes containing electron-donating or electron-withdrawing substituent groups and long-chain alkynes, has been examined (Table 1). To our delight, all these alkynes can be converted to the corresponding alkenes with remarkably high conversion (>99 %) and selectivity (94–98 %). These results manifest the potentially wide capability of $PdCu_2$@MF–CH_3 in the semihydrogenation of terminal alkynes with negligible influence by the substituent effect of the substrates. In addition, when internal alkynes such as 2-butyne and 1-phenyl-1-propyne are used as substrates, $PdCu_2$@MF–CH_3 still exhibits excellent catalytic activity and selectivity towards the corresponding alkene products. In contrast, poor activity for the hydrogenation of diphenylacetylene is observed, possibly due to the large substrate size yet small pore size of MF–CH_3 (Table S4).

The superior catalytic performance of $PdCu_2$@MF–CH_3 over other $PdCu_2$@MF–X catalysts prompt us to elucidate the internal relationships between the activity and basically the only variable, i.e., the functional group on the COF pore wall in $PdCu_2$@MF–X. To identify the critical role of the secondary microenvironment in the catalytic activity of $PdCu_2$ NPs, CO adsorption diffuse reflectance infrared Fourier transform spectroscopy (CO-DRIFTS) has been adopted to analyse the surface electronic states of Pd species in $PdCu_2$@MF–X. The CO molecule is a well-known sensitive probe of Pd-assembled surface structures, in which a more negatively charged surface would result in a redshift of the CO vibration frequency and *vice versa*.[13] In our case, all four samples display the vibration frequency of linear-bound CO at 2061–2052 cm^{-1} together with the bridge-bound CO peak at 1908–1891 cm^{-1} (Figure 3a).[14] Compared to that in $PdCu_2$@MF–H, the vibration of linearly bonded CO on $PdCu_2$@MF–CH_3 shifts to a lower frequency by 4 cm^{-1}, implying that the Pd electron density in $PdCu_2$@MF–CH_3 is higher than that in $PdCu_2$@MF–H. The reason for this observation may be that the –CH_3 functional group as an electron donor increases the Pd electron density, which successively donates electrons to the 2π* orbitals of CO (electron feedback), resulting in a weaker Pd–CO adsorption and a lower wavenumber of CO vibration.[15] The above CO-DRIFTS data suggest that the Pd species in four COFs possess discriminative electronic states, in which the electron-rich degree of Pd species in $PdCu_2$@MF–X follows

Table 1: Semihydrogenation of diverse terminal alkynes over $PdCu_2$@MF–CH_3.

Entry	Substrate	Product	Conv. [%]	Sel. [%]
1	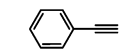	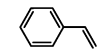	>99	97
2	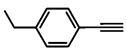	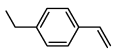	>99	95
3	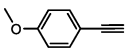	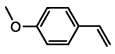	>99	97
4	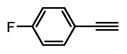	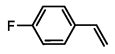	>99	94
5	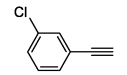	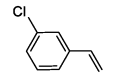	>99	96
6	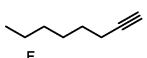	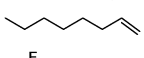	>99	97
7	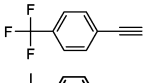	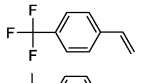	>99	95
8	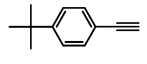	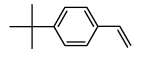	>99	98

Reaction conditions: 0.1 mmol alkyne, 2 mg catalyst, 2 mL MeOH, 15 μL pyridine 30 °C, 1 bar H_2, 4 h. Conversion and selectivity were determined by GC.

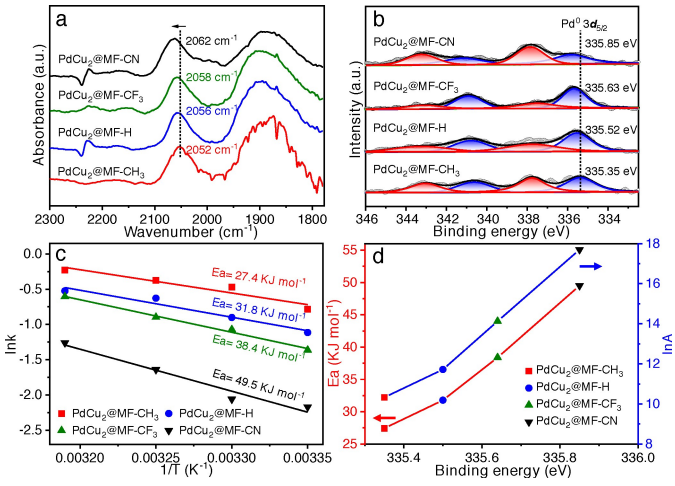

Figure 3. a) The CO-DRIFTS spectra at saturation coverage and b) XPS spectra of Pd 3d for $PdCu_2$@MF–X at 298 K. c) Arrhenius plots and related activation energies for the conversion in the hydrogenation of phenylacetylene over $PdCu_2$@MF–X. d) The relationship between E_a (left *y*-axis) and lnA (right *y*-axis) and the binding energy of Pd $3d_{5/2}$ for $PdCu_2$@MF–X.

the trend of $PdCu_2$@MF–CH_3 > $PdCu_2$@MF–H > $PdCu_2$@MF–CF_3 > $PdCu_2$@MF–CN.

The X-ray photoelectron spectroscopy (XPS) measurements have been further conducted to unveil the Pd electronic state in $PdCu_2$@MF–X (Figure 3b). The four catalysts exhibit two sets of peaks ascribed to Pd^0 and Pd^{2+} in the binding energy range of 334–344 eV.[16] The presence of Pd^{2+} indicates that the samples may be partially oxidized under air due to the tiny $PdCu_2$ sizes. The Pd^0 $3d_{5/2}$ peak appears at a binding energy of 335.35 eV in $PdCu_2$@MF–CH_3, which is decreased by 0.17 eV compared to that in $PdCu_2$@MF–H. This negative shift of the Pd^0 $3d_{5/2}$ binding energy suggests that the Pd sites in $PdCu_2$@MF–CH_3 are more electron-rich than those in $PdCu_2$@MF–H due to the electron donation effect of the –CH_3 group to Pd.[17] In contrast, electron-deficient Pd species are involved in $PdCu_2$@MF–CN and $PdCu_2$@MF–CF_3 featuring electron-withdrawing groups, for which the binding energy of Pd^0 $3d_{5/2}$ shifts to higher values than that for $PdCu_2$@MF–H. In line with the CO-DRIFTS results, the XPS data further demonstrate that the electron-rich degree of Pd species in $PdCu_2$@MF–X follows the electron-donating ability order of the anchored groups in the corresponding COFs well. In addition, the binding energy of Pd^0 $3d_{5/2}$ in $PdCu_2$@MF–CH_3 is positively shifted by approximately 0.1 eV compared to that in Pd@MF–CH_3 (Figure S16), supporting the Cu–Pd interaction and electron transfer from Pd to Cu species.

To gain insights into the relationship between the Pd electronic state and catalytic activity, kinetics experiments have been carried out for $PdCu_2$@MF–X. First, the apparent activation energy (E_a) of $PdCu_2$@MF–X is evaluated by kinetic experiments at different temperatures. The optimized $PdCu_2$@MF–CH_3 exhibits the lowest activation energy of 27.4 kJ mol^{-1}, which is apparently lower than that in the other three catalysts, which are 31.8, 38.4, and 49.5 kJ mol^{-1} for $PdCu_2$@MF–H, $PdCu_2$@MF–CF_3, and $PdCu_2$@MF–CN, respectively (Figure 3c). Unexpectedly, the activation energy demonstrates an almost linear dependence on the binding energy of Pd $3d_{5/2}$ (Figure 3d, red plot). This indicates that the enriched electron density of the Pd surface would be favorable to promote the activation of reaction species toward the production of styrene. Moreover, the natural logarithm of the Arrhenius preexponential factor A (ln A) is further compared (Figure 3d, blue plot), which also delivers an almost linear dependence on the binding energy of Pd $3d_{5/2}$. According to transition state theory, the preexponential factor A mainly reflects the freedom loss of reactants upon adsorption over the catalyst surface. In this regard, $PdCu_2$@MF–CH_3 with the lowest ln A should have the strongest steric constraints for the reactants due to the catalyst surface interactions with chemisorbed species. Accordingly, the bound state for the adsorbed phenylacetylene is suggested to be increased on $PdCu_2$@MF–CH_3 with the highest Pd electron density to promote its activation, thereby contributing to its highest activity.

To further explore the mechanism of the semihydrogenation of phenylacetylene over $PdCu_2$@MF–CH_3, DRIFTS measurements are executed to monitor the conversion of phenylacetylene over $PdCu_2$@MF–CH_3 (Figure 4a). The

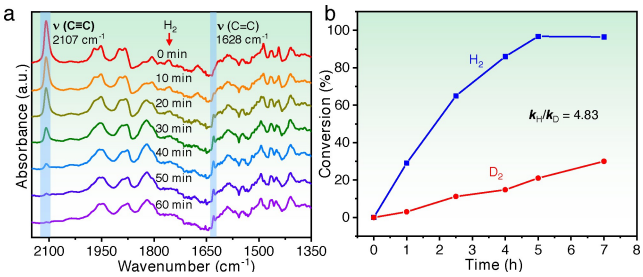

Figure 4. a) Monitoring the catalytic semihydrogenation process of phenylacetylene over $PdCu_2$@MF–CH_3 in the presence of pyridine by using *in situ* DRIFT spectra. b) Primary isotope effect observed for the semihydrogenation of phenylacetylene over $PdCu_2$@MF–CH_3.

signal of C≡C at 2107 cm^{-1} gradually disappears with the introduction of H_2, meanwhile the adsorption peak of C=C from the product styrene at 1628 cm^{-1} steadily increases. When phenylacetylene is completely consumed, the adsorption strength of styrene remains unchanged, which indicates that styrene is not further hydrogenated. In contrast, for the phenylacetylene hydrogenation over Pd@MF–CH_3, the signal of styrene at 1628 cm^{-1} is hardly observed (Figure S17), which illustrates the rapid conversion of styrene to over-hydrogenated phenylethane in the reaction, highlighting the significant role of Cu species as the primary microenvironment in improving the Pd hydrogenation selectivity. Furthermore, the adsorption behavior of $PdCu_2$@MF–CH_3 for styrene with the introduction of H_2 is also examined based on DRIFTS, in which the adsorption strength of styrene at 1628 cm^{-1} remains unchanged (Figure S18), well supporting that styrene is not further hydrogenated over $PdCu_2$@MF–CH_3. In addition, ^{1}H nuclear magnetic resonance (NMR) with deuterium-labelled reagents is performed to identify the hydrogen source. When CH_3OD is used as the reaction solvent, no deuterium-substituted hydrogenation product can be detected, indicating that the solvent does not participate in the hydrogenation process (Figure S19).[18] In contrast, when the reaction gas H_2 is replaced by D_2, the peak ratios of the three ethylene protons at 6.75, 5.75, and 5.25 ppm in the product significantly change from the theoretical value of 1:1:1 to a value of 1:5:1 due to deuterium addition (Figure S20). The results clearly support that the hydrogen source of this reaction is indeed hydrogen gas.

The experimental isotope effect is then studied to assess the mode of hygrogen dissociation on supported $PdCu_2$ NPs. A large kinetic isotope effect (KIE) of 4.83 is observed in the semihydrogenation of phenylacetylene over $PdCu_2$@MF–CH_3 (Figure 4b), which supports the heterolytic activation pathway of H_2, suggesting the involvement of proton transfer in the subsequent hydrogenation steps.[19] With the experimental results above, it is safe to propose a mechanism for the pyridine-involved semihydrogenation of phenylacetylene over $PdCu_2$ NPs, in which heterolytic H_2 activation occurs at $PdCu_2$ NPs (Figure S21).

To elucidate the influence of the Cu in $PdCu_2$ NPs on the reaction selectivity to styrene, DFT calculations have been carried out on the Cu (111), Pd (111), and $PdCu_2$ (111)

surfaces (Figure S22). Compared with Pd (111), the *d*-band center of $PdCu_2$ (111) shifts down by 0.32 eV (Figure 5a). In the optimized structures, the C=C bond of styrene on the surface of Pd (111) is 1.445 Å, with both C atoms adsorbed on two adjacent Pd atoms. However, the C=C bond of styrene on the surface of $PdCu_2$ (111) is 1.406 Å, with only one C atom in the C=C bond adsorbed on each Pd atom (Table S5). Therefore, the configuration of styrene is less favored for hydrogenation on $PdCu_2$ (111) than on Pd (111). Meanwhile, the adsorption energy of styrene on $PdCu_2$ (111) is −2.85 eV, 1.04 eV smaller than that on Pd (111), which is detrimental to further hydrogenation (Figure 5b). Overall, the introduction of Cu to Pd effectively reduces the adsorption energy of styrene and increases the activation energy of overhydrogenation, which would be jointly responsible for the improved selectivity.

The influence of different groups (–CN, $–CF_3$, –H, and $–CH_3$) of COFs, behaving as the secondary microenvironment, on the reactivity of $PdCu_2$ sites has also been investigated by analysing their partial density of states (PDOS) based on the built COF models (Figures 5c, S23). The calculated PDOS maps show that the conduction bands of MF–CN and MF–CF_3 are close to the Fermi level, while for MF–H and MF–CH_3, their valence bands are close to the Fermi level. These results suggest that MF–CN and MF–CF_3 are prone to accept electrons, and in contrast, MF–H and MF–CH_3 are inclined to lose electrons. The electron loss trend follows the order of MF–CH_3 > MF–H > MF–CF_3 > MF–CN. The Bader charge is adopted to identify the electron transfer ability between $PdCu_2$ and four different groups (–CN, $–CF_3$, –H, and $–CH_3$). Simplified models of the benzene ring with four different substituents positioned in the vicinity of $PdCu_2$ (2–3 Å, Figure S24) are constructed and utilized. The calculated Bader charge distribution shows that prominent electron accumulation occurs around the –CN group, while near the $–CH_3$ group, no significant electron accumulation can be observed (Figure 5d). The above PDOS calculation and Bader charge analysis results support that different functional groups on the pore wall of MF–X can profoundly affect the charge donating or withdrawing ability of the corresponding COFs. This will influence the charge transfer between MF–X and $PdCu_2$ NPs that are likely in close proximity to each other in $PdCu_2$@MF–X. Therefore, MF–CH_3 with a strong electron donating group will cause the most pronounced electron transfer from the MF–X to $PdCu_2$ NPs, leading to the most negative Pd electronic state.

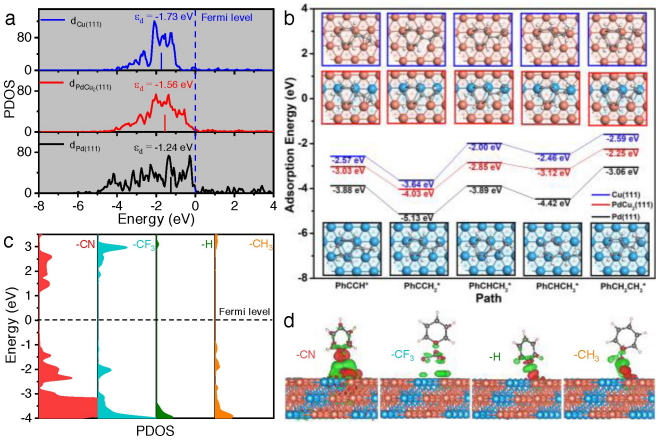

Figure 5. a) Projected density of states (PDOS) of the *d*-bands of Cu (111), $PdCu_2$ (111) and Pd (111) surfaces. b) Adsorption energies of step-by-step hydrogenation of phenylacetylene to styrene at Cu (111), $PdCu_2$ (111) and Pd (111) surfaces. c) PDOS profiles for the MF–X containing –CN, $–CF_3$, –H and $–CH_3$ groups (from left to right). d) Bader charge analysis of $PdCu_2$ surrounding the four different groups: –CN, $–CF_3$, –H and $–CH_3$ (from left to right). Orange, sky blue, gray and white spheres represent Cu, Pd, C and H atoms, respectively. Green and red spheres represent charge depletion and accumulation (± 0.003 e Å^{-3}), respectively.

Conclusion

In summary, ultrafine bimetallic $PdCu_2$ NPs have been encapsulated by COFs with substituent groups to afford $PdCu_2$@MF–X (X = $–CH_3$, –H, $–CF_3$, and –CN) for the selective semihydrogenation of alkynes. The selectivity of Pd sites is greatly improved by primary (coordination) microenvironment modulation by alloying Cu with the addition of pyridine. The electronic state of Pd sites is optimized by encapsulating the $PdCu_2$ NPs into COFs featuring engineered pore walls dangling with diverse –X functional groups, serving as the secondary microenvironment modulation, which gives rise to discriminative activity. As a result, the optimized $PdCu_2$@MF–CH_3 with an enriched Pd electronic state exhibits the highest activity and satisfactory selectivity (97 %) for the target olefins in the semihydrogenation of alkynes. This work provides significant inspiration for the design of heterogeneous catalysts and opens up a new avenue for the rational control of the multilevel chemical microenvironment surrounding active metal sites to optimize catalytic performance.

Acknowledgements

This work was supported by the National Key Research and Development Program of China (2021YFA1500402), the Strategic Priority Research Program of the Chinese Academy of Sciences (XDB0450302), National Natural Science Foundation of China (U22A20401, 22161142001, and 22101269), and Fundamental Research Funds for the Central Universities (WK3450000007, WK2060000038).

Conflict of Interest

The authors declare no conflict of interest.

Data Availability Statement

The data that support the findings of this study are available from the corresponding author upon reasonable request.

Keywords: Covalent-Organic Frameworks · Heterogeneous Catalysis · Hydrogenation · Metal Nanoparticles · Microenvironment Modulation

[1] a) D. Teschner, J. Borsodi, A. Wootsch, Z. Révay, M. Hävecker, A. Knop-Gericke, S. D. Jackson, R. Schlögl, *Science* **2008**, *320*, 86–89; b) D. Albani, M. Shahrokhi, Z. Chen, S. Mitchell, R. Hauert, N. López, J. Pérez-Ramírez, *Nat. Commun.* **2018**, *9*, 2634; c) Q. Feng, S. Zhao, Y. Wang, J. Dong, W. Chen, D. He, D. Wang, J. Yang, Y. Zhu, H. Zhu, L. Gu, Z. Li, Y. Liu, R. Yu, J. Li, Y. Li, *J. Am. Chem. Soc.* **2017**, *139*, 7294–7301; d) Y. Li, K. Yan, Y. Cao, X. Ge, X. Zhou, W. Yuan, D. Chen, X. Duan, *ACS Catal.* **2022**, *12*, 12138–12161; e) L. M. Zhao, X. T. Qin, X. R. Zhang, X. B. Cai, F. Huang, Z. M. Jia, J. Y. Diao, D. Q. Xiao, Z. Jiang, R. F. Lu, N. Wang, H. Y. Liu, D. Ma, *Adv. Mater.* **2022**, *34*, 2110455; f) L. Zhang, M. Zhou, A. Wang, T. Zhang, *Chem. Rev.* **2020**, *120*, 683–733; g) C. W. A. Chan, A. H. Mahadi, M. M.-J. Li, E. C. Corbos, C. Tang, G. Jones, W. C. H. Kuo, J. Cookson, C. M. Brown, P. T. Bishop, S. C. E. Tsang, *Nat. Commun.* **2014**, *5*, 5787.

[2] a) G. Kyriakou, M. B. Boucher, A. D. Jewell, E. A. Lewis, T. J. Lawton, A. E. Baber, H. L. Tierney, M. Flytzani-Stephanopoulos, E. C. H. Sykes, *Science* **2012**, *335*, 1209–1212; b) G. X. Pei, X. Y. Liu, X. Yang, L. Zhang, A. Wang, L. Li, H. Wang, X. Wang, T. Zhang, *ACS Catal.* **2017**, *7*, 1491–1500; c) H. Xin, A. Vojvodic, J. Voss, J. K. Nørskov, F. Abild-Pedersen, *Phys. Rev. B* **2014**, *89*, 867–875.

[3] a) Q.-L. Zhu, Q. Xu, *Chem* **2016**, *1*, 220–245; b) R. J. White, R. Luque, V. L. Budarin, J. H. Clark, D. J. Macquarrie, *Chem. Soc. Rev.* **2009**, *38*, 481–494; c) A. Dhakshinamoorthy, H. Garcia, *Chem. Soc. Rev.* **2012**, *41*, 5262–5284.

[4] a) L. Lu, S. Zou, B. Fang, *ACS Catal.* **2021**, *11*, 6020–6058; b) L. Zhang, Z. Wei, S. Thanneeru, M. Meng, M. Kruzyk, G. Ung, B. Liu, J. He, *Angew. Chem. Int. Ed.* **2019**, *58*, 15834–15840.

[5] a) Q. Yang, Q. Xu, H.-L. Jiang, *Chem. Soc. Rev.* **2017**, *46*, 4774–4808; b) K. Choe, F. Zheng, H. Wang, Y. Yuan, W. Zhao, G. Xue, X. Qiu, M. Ri, X. Shi, Y. Wang, G. Li, Z. Tang, *Angew. Chem. Int. Ed.* **2020**, *59*, 3650–3657; c) J. Zhang, L. Wang, Y. Shao, Y. Wang, B. C. Gates, F.-S. Xiao, *Angew. Chem. Int. Ed.* **2017**, *56*, 9747–9751; d) S. Wang, Z. J. Zhao, X. Chang, J. Zhao, H. Tian, C. Yang, M. Li, Q. Fu, R. Mu, J. Gong, *Angew. Chem. Int. Ed.* **2019**, *58*, 7668–7672; e) X. Zhu, Q. Guo, Y. Sun, S. Chen, J. Q. Wang, M. Wu, W. Fu, Y. Tang, X. Duan, D. Chen, Y. Wan, *Nat. Commun.* **2019**, *10*, 1428; f) X. Yang, J.-K. Sun, M. Kitta, H. Pang, Q. Xu, *Nat. Catal.* **2018**, *1*, 214–220.

[6] a) Y. Cao, Z. Sui, Y. Zhu, X. Zhou, D. Chen, *ACS Catal.* **2017**, *7*, 7835–7846; b) R. Gao, J. Xu, J. Wang, J. Lim, C. Peng, L. Pan, X. Zhang, H. Yang, J. Zou, *J. Am. Chem. Soc.* **2022**, *144*, 573–581.

[7] a) A. P. Côté, A. I. Benin, N. W. Ockwig, M. O'Keeffe, A. J. Matzger, O. M. Yaghi, *Science* **2005**, *310*, 1166–1170; b) Z. Wang, S. Zhang, Y. Chen, Z. Zhang, S. Ma, *Chem. Soc. Rev.* **2020**, *49*, 708–735; c) K. Geng, T. He, R. Liu, S. Dalapati, K. T. Tan, Z. Li, S. Tao, Y. Gong, Q. Jiang, D. Jiang, *Chem. Rev.* **2020**, *120*, 8814–8933; d) X. Guan, H. Li, Y. Ma, M. Xue, Q. Fang, Y. Yan, V. Valtchev, S. Qiu, *Nat. Chem.* **2019**, *11*, 587–594; e) Z. Zhang, C. Kang, S. Peh, D. Shi, F. Yang, Q. Liu, D. Zhao, *J. Am. Chem. Soc.* **2022**, *144*, 14992–14996; f) S. Zhang, G. Cheng, L. Guo, N. Wang, B. Tan, S. Jin, *Angew. Chem. Int. Ed.* **2020**, *59*, 6007–6014; g) Y. Zeng, R. Zou, Y. Zhao, *Adv. Mater.* **2016**, *28*, 2855–2873; h) S.-Y. Ding, W. Wang, *Chem. Soc. Rev.* **2013**, *42*, 548–568; i) S. Yang, W. Hu, X. Zhang, P. He, B. Pattengale, C. Liu, M. Cendejas, I. Hermans, X. Zhang, J. Zhang, J. Huang, *J. Am. Chem. Soc.* **2018**, *140*, 14614–14618.

[8] a) M. Lu, M. Zhang, J. Liu, T.-Y. Yu, J.-N. Chang, L.-J. Shang, S.-L. Li, Y.-Q. Lan, *J. Am. Chem. Soc.* **2022**, *144*, 1861–1871; b) S. L. Lu, Y. M. Hu, S. Wan, R. McCaffrey, Y. H. Jin, H. W. Gu, W. Zhang, *J. Am. Chem. Soc.* **2017**, *139*, 17082–17088; c) Q. Guan, L.-L. Zhou, Y.-B. Dong, *Chem. Soc. Rev.* **2022**, *51*, 6307–6416; d) M. Guo, S. Jayakumar, M. Luo, X. Kong, C. Li, H. Li, J. Chen, Q. Yang, *Nat. Commun.* **2022**, *13*, 1770; e) S. Ding, J. Gao, Q. Wang, Y. Zhang, W. Song, C. Su, W. Wang, *J. Am. Chem. Soc.* **2011**, *133*, 19816–19822; f) P. Pachfule, M. K. Panda, S. Kandambeth, S. M. Shivaprasad, D. D. Díaz, R. Banerjee, *J. Mater. Chem. A* **2014**, *2*, 7944–7952; g) P. Pachfule, S. Kandambeth, D. D. Díaz, R. Banerjee, *Chem. Commun.* **2014**, *50*, 3169–3172; h) S. B. Kalidindi, H. Oh, M. Hirscher, D. Esken, C. Wiktor, S. Turner, G. Van Tendeloo, R. A. Fischer, *Chem. Eur. J.* **2012**, *18*, 10848–10856.

[9] X. Li, C. Zhang, S. Cai, X. Lei, V. Altoe, F. Hong, J. J. Urban, J. Ciston, E. M. Chan, Y. Liu, *Nat. Commun.* **2018**, *9*, 2998.

[10] a) Y. Hu, N. Goodeal, Y. Chen, A. M. Ganose, R. G. Palgrave, H. Bronstein, M. O. Blunt, *Chem. Commun.* **2016**, *52*, 9941–9944; b) W. J. Gammon, O. Kraft, A. C. Reilly, B. C. Holloway, *Carbon* **2003**, *41*, 1917–1923.

[11] Y.-Z. Chen, B. Gu, T. Uchida, J. Liu, X. Liu, B.-J. Ye, Q. Xu, H.-L. Jiang, *Nat. Commun.* **2019**, *10*, 3462.

[12] a) I. Schrader, J. Warneke, J. Backenkohler, S. Kunz, *J. Am. Chem. Soc.* **2015**, *137*, 905–912; b) J. L. Fiorio, N. López, L. M. Rossi, *ACS Catal.* **2017**, *7*, 2973–2980.

[13] M. R. Ball, K. R. Rivera-Dones, E. B. Gilcher, S. F. Ausman, C. W. Hullfish, E. A. Lebron, J. A. Dumesic, *ACS Catal.* **2020**, *10*, 8567–8581.

[14] a) W.-K. Qin, D.-H. Si, Q. Yin, X.-Y. Gao, Q.-Q. Huang, Y.-N. Feng, L. Xie, S. Zhang, X.-S. Huang, T.-F. Liu, R. Cao, *Angew. Chem. Int. Ed.* **2022**, *61*, e202202089; b) Y. Li, W. S. Lo, F. Zhang, X. Si, L. Y. Chou, X. Y. Liu, B. P. Williams, Y. H. Li, S. H. Jung, Y. S. Hsu, F. S. Liao, F. K. Shieh, M. N. Ismail, W. Huang, C. K. Tsung, *J. Am. Chem. Soc.* **2021**, *143*, 5182–5190.

[15] X. Li, T. Goh, L. Li, C. Xiao, Z. Guo, X. Zeng, W. Huang, *ACS Catal.* **2016**, *6*, 3461–3468.

[16] D. Wu, W. Baaziz, B. Gu, M. Marinova, W. Y. Hernández, W. Zhou, E. I. Vovk, O. Ersen, O. V. Safonova, A. Addad, N. Nuns, A. Y. Khodakov, V. V. Ordomsky, *Nat. Catal.* **2021**, *4*, 595–606.

[17] a) D. Chen, W. Yang, L. Jiao, L. Li, S.-H. Yu, H.-L. Jiang, *Adv. Mater.* **2020**, *32*, 2000041; b) L. Jiao, J. Wang, H.-L. Jiang, *Acc. Mater. Res.* **2021**, *2*, 327–339.

[18] L. Li, W. Yang, Q. Yang, Q. Guan, J. Lu, S.-H. Yu, H.-L. Jiang, *ACS Catal.* **2020**, *10*, 7753–7762.

[19] P. X. Liu, Y. Zhao, R. X. Qin, S. G. Mo, G. X. Chen, L. Gu, D. M. Chevrier, P. Zhang, Q. Guo, D. D. Zhang, B. H. Wu, Q. Fu, N. F. Zheng, *Science* **2016**, *352*, 797–801.

Manuscript received: April 13, 2023
Accepted manuscript online: May 2, 2023
Version of record online: May 17, 2023